34. Conformal, molecular-scale contact between PDMS and other materials provides the basis for the family of microcontact printing techniques, whereby molecules (e.g., alkane thiols) are transferred from PDMS stamps onto various substrates (e.g., gold) to form self-assembled monolayers that are densely packed on molecular scales and uniform over large areas. In this and other applications, conformal contact is most readily achieved by curing PDMS prepolymer against atomically flat silica wafers (as in our experiments). For details, see (*45*, *46*).
35. S. Kittaka, *J. Phys. Soc. Jpn.* **14**, 532 (1959).
36. G. M. Sessler, in *Electronic Properties of Polymers*, J. Mort, G. Pfister, Eds. (Wiley, New York, 1982), pp. 59–100.
37. B. B. Mandelbrot, *The Fractal Geometry of Nature* (Freeman, New York, 1983).
38. J. J. Cole, C. R. Barry, X. Wang, H. O. Jacobs, *ACS Nano* **4**, 7492 (2010).
39. G. Socrates, *Infrared and Raman Characteristic Group Frequencies* (Wiley, Chichester, UK, 2001)
40. Y. Israeli, J. Lacoste, J. Cavezzan, J. Lemaire, *Polym. Degrad. Stabil.* **42**, 267 (1993).
41. D. H. Chenery, *Biomaterials* **18**, 415 (1997).
42. W. R. Salaneck, A. Paton, *J. Appl. Phys.* **47**, 144 (1976).
43. J. Lowell, *J. Phys. D Appl. Phys.* **10**, L233 (1977).
44. C. G. Camara, J. V. Escobar, J. R. Hird, S. J. Putterman, *Nature* **455**, 1089 (2008).
45. Y. N. Xia, G. M. Whitesides, *Annu. Rev. Mater. Sci.* **28**, 153 (1998).
46. Y. Xia, D. Qin, G. M. Whitesides, *Adv. Mater.* **8**, 1015 (1996).

Acknowledgments: This work was supported by the Non-Equilibrium Energy Research Center (NERC), which is an Energy Frontier Research Center funded by the U.S. Department of Energy, Office of Science, Office of Basic Energy Sciences under award DE-SC0000989.

Supporting Online Material

www.sciencemag.org/cgi/content/full/science.1201512/DC1
Materials and Methods
SOM Text
Figs. S1 to S4
References

10 December 2010; accepted 19 May 2011
Published online 23 June 2011;
10.1126/science.1201512

Structure of the FANCI-FANCD2 Complex: Insights into the Fanconi Anemia DNA Repair Pathway

Woo Joo,[1]* Guozhou Xu,[2]* Nicole S. Persky,[1,3]* Agata Smogorzewska,[4,5] Derek G. Rudge,[1,3] Olga Buzovetsky,[1,3] Stephen J. Elledge,[3,4] Nikola P. Pavletich[1,3]†

Fanconi anemia is a cancer predisposition syndrome caused by defects in the repair of DNA interstrand cross-links (ICLs). Central to this pathway is the Fanconi anemia I–Fanconi anemia D2 (FANCI-FANCD2) (ID) complex, which is activated by DNA damage–induced phosphorylation and monoubiquitination. The 3.4 angstrom crystal structure of the ~300 kilodalton ID complex reveals that monoubiquitination and regulatory phosphorylation sites map to the I-D interface, suggesting that they occur on monomeric proteins or an opened-up complex and that they may serve to stabilize I-D heterodimerization. The 7.8 angstrom electron-density map of FANCI-DNA crystals and in vitro data show that each protein has binding sites for both single- and double-stranded DNA, suggesting that the ID complex recognizes DNA structures that result from the encounter of replication forks with an ICL.

Fanconi anemia (FA) is a recessive cancer predisposition and developmental syndrome characterized by hypersensitivity to DNA interstrand cross-linking agents (*1*). The proteins mutated in the 13 FA complementation groups act in a common pathway that results in DNA repair by homologous recombination (*2*, *3*). The FA pathway is activated when a DNA replication fork encounters an interstrand cross-link (ICL), although FA proteins can be recruited to ICLs in the absence of DNA replication as well (*4*–*7*).

Central to the FA pathway is the ID complex formed by the FA D2 (FANCD2) and FA I (FANCI) proteins (*8*–*11*). Activation of the pathway culminates in FANCD2 and FANCI phosphorylation by ATR (ataxia telangiectasia and Rad3-related) (*1*, *12*), their monoubiquitination by the FA core complex ubiquitin ligase (*1*, *2*, *13*), and their localization to chromatin foci that are considered sites of repair (*9*, *14*, *15*).

Replication-dependent ICL repair involves nucleolytic incisions flanking the ICL on one strand, translesion DNA synthesis across the unhooked ICL, removal of the ICL by additional incisions, and homologous recombination (*3*–*5*). Depletion of FANCD2 or mutation of its ubiquitination site arrests the process before the initial incision step (*5*). Among the nucleases implicated in these incisions, FAN1 and SLX4-SLX1 contain a ubiquitin-binding UBZ domain required for their association with monoubiquitinated ID (*3*, *16*).

FANCI and FANCD2 consist of 1328 and 1451 amino acids, respectively. They share a ~150–amino acid region of homology around their monoubiquitination sites, and they have been proposed to be paralogs (*17*). Neither protein has any recognizable sequence motifs. They have been shown to bind to DNA, although the nature of their specific DNA substrates has not been clear (*18*–*20*).

Here, we present the 3.4 Å crystal structure of the 296 kD ID complex, the 3.3 Å structure of individual FANCI, as well as the 7.8 Å crystallographic electron-density map of a FANCI protein bound to a splayed Y DNA.

Overall structure of the ID complex. Crystals were grown using mouse FANCI (residues 1 to 1301) and FANCD2 (residues 33 to 1415) proteins that were truncated to remove regions highly susceptible to proteolysis (figs. S1 and S2).

The structures of FANCI and FANCD2 have overall similar shapes and share extensive local similarity essentially throughout their length (Fig. 1A and fig. S3). They consist predominantly of α helices, the majority of which are arranged in antiparallel pairs that form α-α superhelical structural segments, commonly referred to as α solenoids. Each structure has four distinct α solenoid segments that range in size from 156 to 310 residues (solenoids 1 to 4) (Fig. 1A and fig. S4). Two other, mostly helical segments intervene between solenoids 1 and 2 (~80-residue helical domain HD1) and between solenoids 2 and 3 (~240-residue HD2) (fig. S4).

FANCI and FANCD2 fold into a saxophone-like structure consisting of a long N-terminal neck (solenoid 1, HD1, and solenoid 2), a U-shaped middle bow (HD2), and a bulbous C-terminal bell (solenoid 3 to solenoid 4) (Fig. 1A and fig. S4). The ID complex has a troughlike shape with partially open ends (Fig. 1, B and C). The interior of the trough, which is ~105 Å long, ~70 Å wide, and ~40 Å deep, is marked by multiple grooves that have a highly positive electrostatic potential. Two of these grooves contain electron density for double-stranded DNA (dsDNA) and single-stranded DNA (ssDNA) in the 7.8 Å map of Y DNA-FANCI crystals (fig. S3C). The FANCD2 Lys^{559} and FANCI Lys^{522} monoubiquitination sites are within the ID interface, in solvent-accessible tunnels located at the bottom of the troughlike structure (Fig. 1A).

The individual solenoid and HD segments of FANCI and FANCD2 share extensive structural homology, although the entire structures cannot be superimposed because of the cumulative effects of differences in individual segments and in intersegment packing arrangements. The most homologous are the solenoid 2 segments, which contain the monoubiquitination sites and the reported FANCI-FANCD2 sequence homology. They can be superimposed with a 1.7 Å Cα root mean square deviation for ~82% of their residues (table S2 and fig. S4B). For the remainder of the segments, the fraction of the superimposing residues ranges from ~66% for solenoid 4 to ~60% for HD2 (table S2). These local and global structural similarities indicate that FANCI and FANCD2

[1]Structural Biology Program, Memorial Sloan-Kettering Cancer Center, New York, NY 10065, USA. [2]Sloan-Kettering Division, Joan and Sanford I. Weill Graduate School of Medical Sciences, Cornell University, New York, NY 10065, USA. [3]Howard Hughes Medical Institute, Memorial Sloan-Kettering Cancer Center, New York, NY 10065, USA. [4]Department of Genetics, Harvard Medical School, Division of Genetics, Brigham and Women's Hospital, Boston, MA 02115, USA. [5]Laboratory of Genome Maintenance, The Rockefeller University, New York, NY 10065, USA.

*These authors contributed equally to this work.
†To whom correspondence should be addressed. E-mail: pavletin@mskcc.org

evolved from a common ancestor [fig. S4 and supporting online material (SOM) text].

Ten of the 11 FA-I and FA-D2 missense mutations (*21*) map to buried residues with clear structure-stabilizing roles, indicating that their pathogenic effects result from structural defects in the mutant proteins (fig. S5).

I-D interface. The two proteins interact along the long dimension of their saxophonelike shape (solenoid 1, HD1, solenoid 2, and part of HD2) in an antiparallel, twofold pseudosymmetric manner (Fig. 2A and fig. S4A). The interface extends along a ~560-residue region on each protein and buries a total of ~7100 Å^2 of solvent-accessible area. It is nearly continuous, except for gaps at the monoubiquitination site of each protein and an additional gap at the center of pseudosymmetry (between opposing HD1 segments).

The interface has comparable numbers of hydrophobic (42 side chains) and polar (44 side chain and 11 backbone groups) residues within intermolecular-contact distance (Fig. 2A; contacts marked on fig. S1). Most of these contacts are clustered near the ends of the extended interface, although with substantial asymmetry in the density of contacts at the two ends. The end where the FANCD2 solenoid 1 packs with the FANCI solenoid 2–HD2 segments has 60 residues involved in contacts (Fig. 2B), compared with only 30 at the reciprocal end (Fig. 2C). This asymmetry results primarily from two structurally nonhomologous regions. One of these involves the N-terminal portions of solenoid 1 segments (hereafter referred to as "caps") (fig. S4), with the FANCD2 cap having 11 contact residues (Fig. 2B) compared with only 2 for the FANCI cap at the reciprocal end (Fig. 2C). The other involves a FANCI-specific HD2 insertion with nine side chain and backbone groups that contact FANCD2 (α26b-α26c) (Fig. 2B, bottom). The asymmetry in these elements and their intermolecular contacts might have evolved to drive the duplicated ancestral protein to form heterodimers instead of homodimers.

The remaining intermolecular contacts are scattered in small groups throughout the porous middle portion of the interface, except around the ubiquitination-site lysine residues, which make no contacts (Fig. 2A and fig. S6).

Monoubiquitination sites. Although the FANCI Lys^{522} and FANCD2 Lys^{559} side chains are embedded in the I-D interface (Fig. 1A), the absence of I-D contacts next to each results in two tunnels (one for each lysine residue) that allow free access to bulk solvent from either side of the trough wall. In the monomeric proteins, both lysine side chains are fully solvent-exposed.

The solvent-accessible tunnels of both sites are wide enough (~7 to 9 Å) and short enough to accommodate the four–amino acid ubiquitin tail, whose C terminus would be covalently linked to the lysine epsilon amino group (Fig. 3, A and B, and fig. S7). The ubiquitin tail is conformationally flexible (*22*), which should aid in its ability to navigate the tunnels, whereas the ubiquitin structural domain is positioned outside the interface. It is also possible, however, that ubiquitination induces a conformational change or a rearrangement of the complex that fully exposes the monoubiquitination sites.

In principle, the tunnels can accommodate a ubiquitin residing either at the trough interior or exterior. The tunnel entrance at the trough interior ("top" entrance looking down the plane of Fig. 1A) is ~13 Å away from the lysine epsilon amino group. The entrance at the "bottom" is farther away at ~17 Å, although the relatively more open, funnel shape of this entrance could also accommodate part of the ubiquitin structural domain (Fig. 3, A and B, fig. S7, and SOM text).

Irrespective of where the ubiquitin is positioned, the dimensions of the tunnels and entrances suggest that the ubiquitin tail and structural domains may contact both their conjugated protein and its heterodimerization partner. As these interactions would be repeated in a reciprocal fashion, the structure raises the possibility that ubiquitination may contribute to the stability of the ID complex. In this respect, we note that the mouse ID complex has a short half-life, as it dissociates during gel filtration chromatography at concentrations of ≤1 μM (fig. S8).

Although the tunnels can readily accommodate the ubiquitin tail, they are too small for the active site of the ubiquitin-conjugating (E2) en-

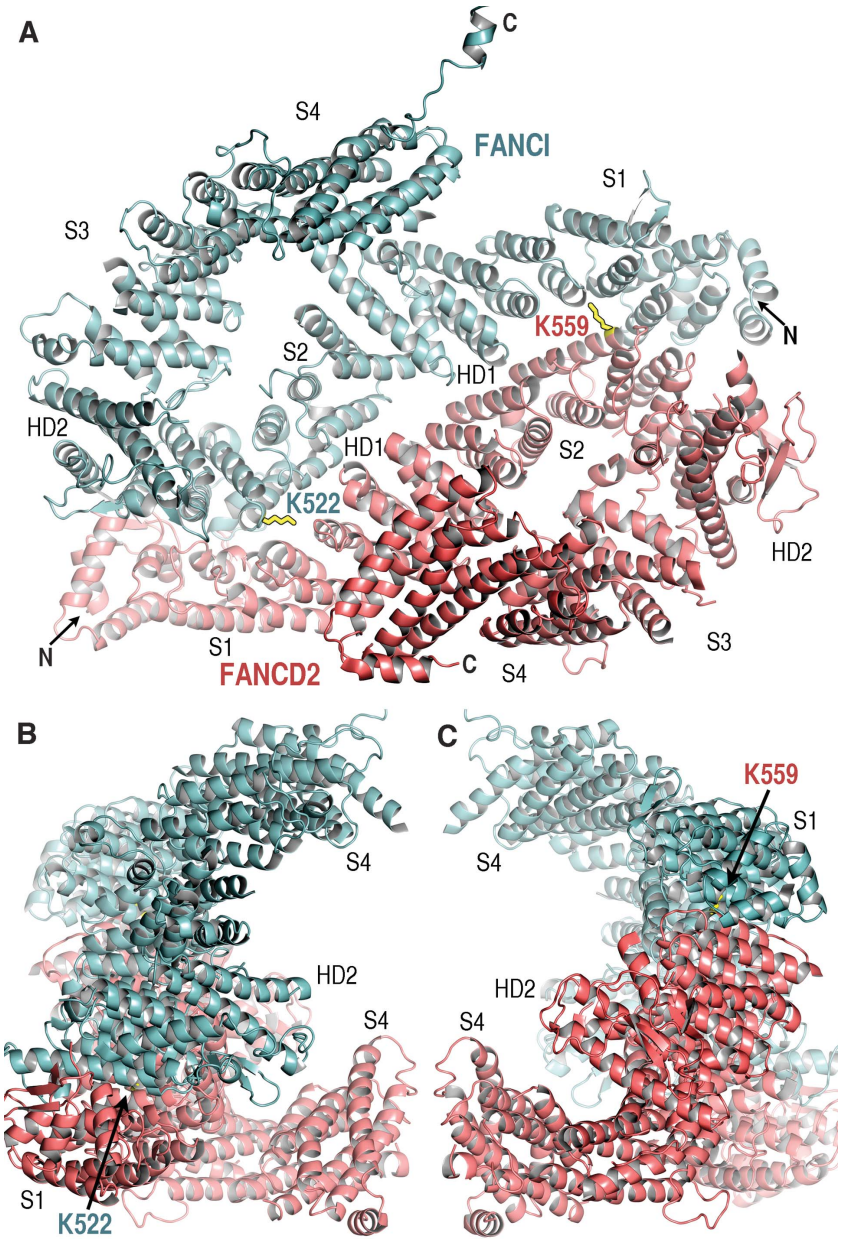

Fig. 1. The overall structure of the ID complex. (**A**) View looking into the interior of the troughlike structure. The FANCI (light blue) and FANCD2 (pink) solenoid (S1 to S4), HD1, and HD2 domains are labeled near their centers. The ubiquitination-site lysine side chains are shown in yellow and outlined in black. The FANCD2 Lys^{559} (K559) side chain is poorly ordered. (**B**) View orthogonal to (A) looking down the left end. Only the segments closest to the viewer are labeled. (**C**) View orthogonal to (A) looking down the right end.

zyme to access the lysine side chains. The structure thus suggests that ubiquitination either occurs on a cellular pool of monomeric FANCI and FANCD2, or it involves a process that opens up the I-D interface.

The sequestration of the lysine-ubiquitin isopeptide bond at the I-D interface would also protect it against de-ubiquitination by the FA-associated USP1 ubiquitin protease (*23*). Coupled to a possible role of ubiquitination stabilizing I-D association, this may explain why cells lacking either FANCI or FANCD2 exhibit loss or reduction of the ubiquitinated form of the paralog (*9*).

Phosphorylation sites. It has been suggested that DNA-damage–dependent phosphorylation of FANCI acts as a molecular switch that activates the pathway, as multiple alanine substitutions at putative phosphorylation sites impede the monoubiquitination and chromatin association of both FANCI and FANCD2 (*12*). Three phosphorylation sites have the ataxia telangiectasia mutated/ATR kinase consensus and are also conserved in vertebrates (Ser^{555}, Thr^{558}, Thr^{564} in mouse FANCI) (fig. S9).

These three sites map to the 37–amino acid FANCI-specific HD2 insertion at the I-D interface. This region undergoes a complete conformational change on FANCD2 binding. In free FANCI, it forms the β3-β4 sheet, and part of it is disordered. In the ID complex, it instead forms two new helices (α26b and α26c) and a 10-residue extension to α27, becoming ordered in its entirety (Fig. 3C). This changes entirely the structural context of the phosphorylation sites. In free FANCI, they map to the disordered segment where they can be readily phosphorylated. In the complex, they end up at the start, middle, and immediately after the α26c helix. Their side chains are embedded in hydrogen bond networks that anchor α26c in the FANCI structure and also contact FANCD2 (Fig. 3D and Fig. 2B, bottom panel). The structure suggests that their phosphorylation may augment the intramolecular hydrogen bond networks, stabilizing the FANCD2-bound conformation of this region, and may also result in new FANCD2 contacts (SOM text and fig. S9 legend). These two effects may cooperate to stabilize I-D association. The magnitude of this stabilization could, in principle, be substantial, as the FANCI α26b-α26c-α27 segment accounts for ~27% of the total solvent accessible area buried on complex formation (Fig. 2, A and B).

The model of phosphorylation stabilizing I-D association, thereby protecting against de-

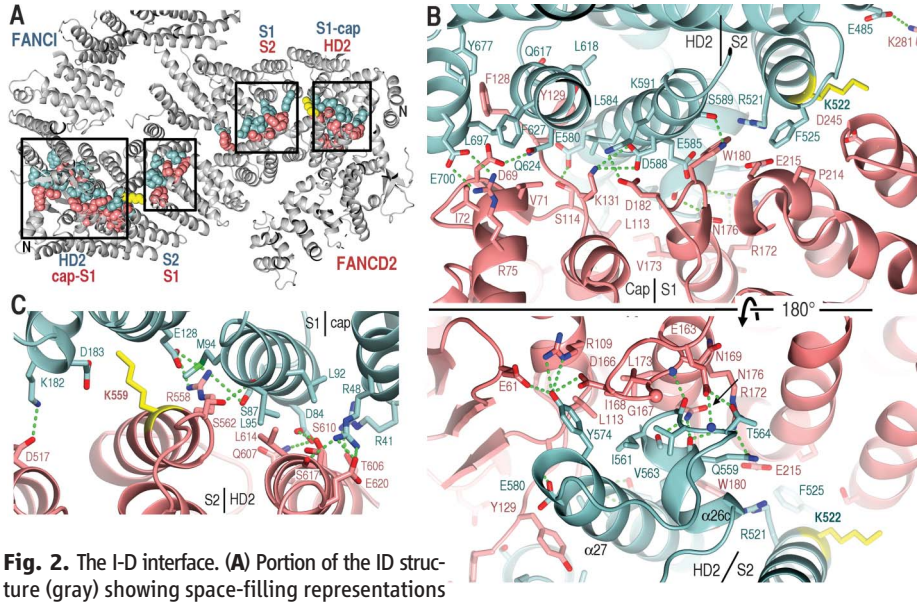

Fig. 2. The I-D interface. (**A**) Portion of the ID structure (gray) showing space-filling representations of side chains within intermolecular-contact distance. Boxes indicate clusters of contacts with their respective segments labeled. (**B**) Close-up view of the FANCD2 cap–solenoid 1 and FANCI solenoid 2–HD2 segments showing side chains from (A) (*24*). Green dotted lines indicate heteroatoms within hydrogen bonding distance and geometry. Top panel orientation is similar to (A), with the bottom panel rotated ~180° about the horizontal axis. The approximate boundaries of segments are labeled. (**C**) Reciprocal end of the interface formed by the FANCI cap–solenoid 1 and FANCD2 solenoid 2–HD2 segments.

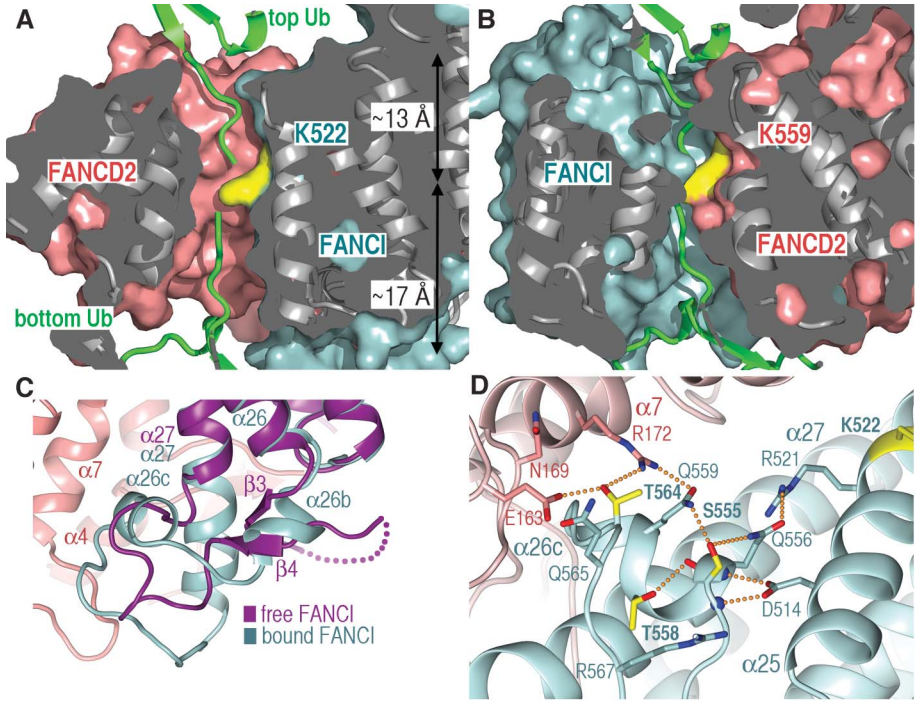

Fig. 3. Monoubiquitination and phosphorylation sites of the ID complex. (**A**) Surface representation of the solvent-accessible tunnel harboring the FANCI Lys^{522} (K522) ubiquitination site, looking from the interface center. The surface portion above the figure plane is clipped, and the surface interior is gray. The approximate distances from the lysine to the tunnel exits are indicated. The free ubiquitin (Ub) structure (green) was manually docked with its tail approaching from either the "top" or "bottom" exits of the tunnel. (**B**) Surface representation of the FANCD2 Lys^{559} tunnel. As in (A), two ubiquitin molecules were docked approaching from either tunnel exit. (**C**) The FANCI Ser^{555}, Thr^{558}, and Thr^{564} phosphorylation sites map to an HD2 segment that undergoes a conformational change between free FANCI (purple) and FANCD2-bound FANCI (light blue). In free FANCI, the three sites map to a disordered loop (dotted purple line). FANCD2 is shown in pink. (**D**) The hydrogen bond network centered on the phosphorylation sites, also showing neighboring residues that may interact with the phosphorylated residues. Orange dotted lines denote heteroatoms within hydrogen bonding distance.

ubiquitination, may explain why mutations in FANCI phosphorylation sites reduce levels of the ubiquitinated forms of both FANCI and FANCD2 (*12*).

Electron-density map of the Y DNA-FANCI complex. FANCD2 and FANCI have been shown to bind to dsDNA with a minor preference for diverse branched DNA structures such as Holliday junction, splayed Y, overhang, and replication fork DNA (*18*–*20*). In cocrystallization experiments with a variety of branched DNA structures, we obtained diffraction-quality crystals of FANCI bound to a splayed Y DNA consisting of a 16–base pair (bp) dsDNA segment and two 20-nucleotide (nt) ssDNA arms. FANCI binds to this Y DNA with a dissociation constant (K_d) of 19 nM, which is ~10-fold tighter than its affinity for either 18-bp dsDNA or 32-nt ssDNA (fig. S10).

The Y DNA-FANCI crystals diffract to 7.8 Å resolution and contain three complexes in the asymmetric unit (table S1). The electron-density map, calculated after threefold noncrystallographic symmetry averaging, shows unambiguously double-helical electron density, which extends throughout the length of a 16-bp ideal B-type DNA model positioned into the map manually (Fig. 4A and fig. S3C).

At one end of the dsDNA, the map shows an undulating tube of continuous electron density that has a shape consistent with one ssDNA segment. We do not observe clear electron density for the second ssDNA segment of the Y DNA, and we presume it is disordered. Consistent with FANCI having only one major site for binding to ssDNA, we find that its affinity for Y DNA is indistinguishable from its affinity for the corresponding 3′ overhang DNA (19 nM K_d for both) (fig. S10).

The dsDNA lies in a groove that has a semicircular cross section (Fig. 4B). The groove is built by solenoid 4 forming one side and solenoid 3 forming the bottom and part of the other side, the remainder of which is completed by portions of HD1, solenoid 2 and HD2. There are seven FANCI regions that are within contact distance to 13 bp of dsDNA (α19b, α20, α35, α40, α42, α44, α46) (Fig. 4, A and B). Most of these regions involve the second helix of individual repeats and, in particular, the N termini of the helices and the loops immediately preceding them. In addition, four loops or helix ends that are disordered in the FANCI and ID structures become at least partially ordered near the DNA (α19b-α20, α33-α34, α36-α37, and α47-α48 loops) (Fig. 4, A and B). The DNA-proximal FANCI segments are rich in conserved basic residues (marked on fig. S1A).

The transition from dsDNA to ssDNA electron density has α19b and α20 abutting the last base pair of the duplex (Fig. 4A). The ~55 Å path of the tubular ssDNA electron density could correspond to ~8 to 11 nts, depending on the ssDNA backbone conformation and extent of base-base stacking. The electron density follows a groove formed by the long α44, α46, and α48 helices of solenoid 4 on one side and by the α15 and α17 helices of HD1 on the other (Fig. 4A and fig. S11). This groove is lined with residues containing basic, hydroxyl, and amide groups, as well as two conserved phenylalanine residues that are fully solvent-exposed (fig. S11).

The polarity of the ssDNA is not clear due to the limited resolution of the map and the proximity of multiple protein elements at the ssDNA/dsDNA junction. In vitro, FANCI exhibits only a minor preference for 3′ overhang (19 nM K_d) over 5′ overhang DNA (40 nM K_d) (fig. S10).

Implications for the DNA-binding activity of the ID complex. The overall shapes and highly positive electrostatic potential of the dsDNA/ssDNA binding grooves of FANCI are conserved in FANCD2 (Fig. 4C, fig S12, and SOM text). Consistent with this observation, FANCD2 binds to dsDNA and ssDNA with affinities comparable to those of FANCI (fig. S10). Taken together, our data suggest that the ID complex has two sets of dsDNA/ssDNA binding sites arranged in a pseudo-twofold symmetric manner (Fig. 4C and fig. S12).

This raises the possibility that the ID complex binds to two dsDNA/ssDNA structures cross-linked by an ICL. The pausing of a replication fork at an ICL has been shown to initially generate a splayed Y DNA structure, with the subsequent advancement of leading strand synthesis to the –1 position of the ICL generating a cross-linked 5′ flap structure (*4*, *5*). If two forks converge onto the ICL from opposite directions, this would result in an ICL flanked by either two 5′ flaps or one Y and one 5′ flap. Both of these would be compatible with the pseudo-twofold symmetric arrangement of dsDNA/ssDNA-binding sites in the ID complex (Fig. 4C), with the ICL residing near the center of pseudosymmetry of the complex. It is also possible that both single- and double-fork events occur in the cell, with the ID complex evolving a certain level of promiscuity to recognize an array of single- and double-Y and 5′ flap DNA structures.

Our data implicate the ID complex in recognizing DNA structures that result from the encounter of replication forks with an ICL. The complex may function in stabilizing and protecting these DNA structures and also in providing specificity for the initial incisions around the ICL by directing the FA-associated nuclease to these sites.

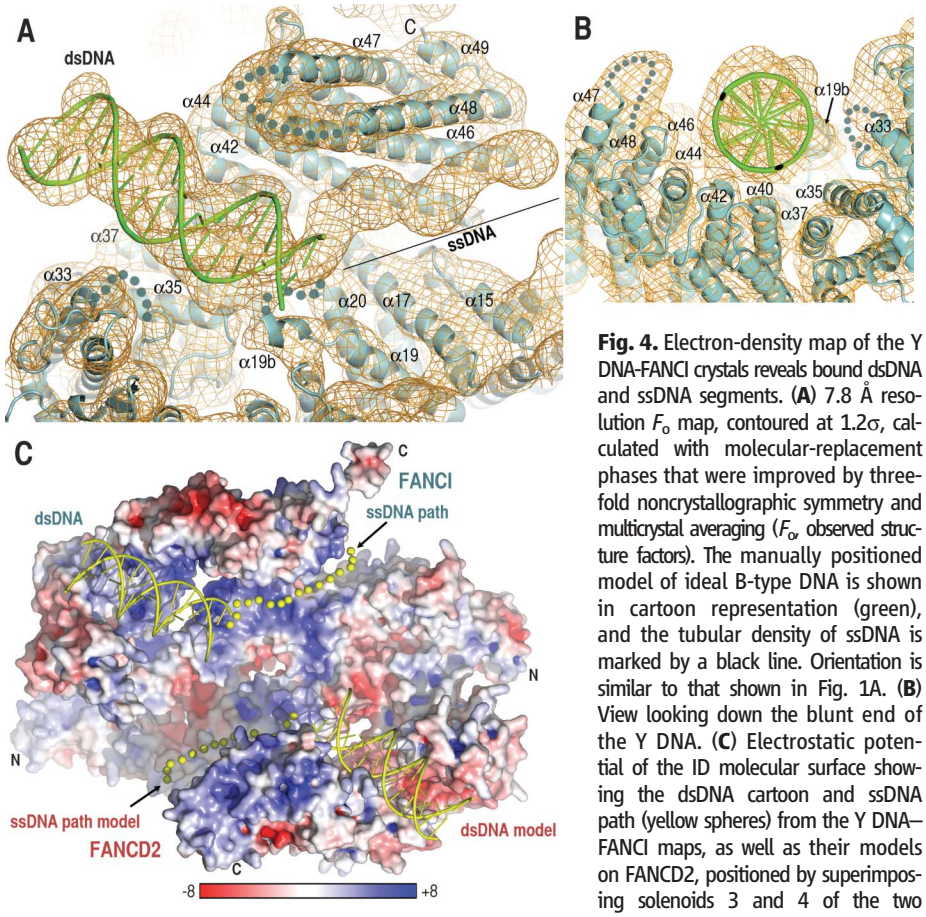

Fig. 4. Electron-density map of the Y DNA-FANCI crystals reveals bound dsDNA and ssDNA segments. (**A**) 7.8 Å resolution F_o map, contoured at 1.2σ, calculated with molecular-replacement phases that were improved by threefold noncrystallographic symmetry and multicrystal averaging (F_o, observed structure factors). The manually positioned model of ideal B-type DNA is shown in cartoon representation (green), and the tubular density of ssDNA is marked by a black line. Orientation is similar to that shown in Fig. 1A. (**B**) View looking down the blunt end of the Y DNA. (**C**) Electrostatic potential of the ID molecular surface showing the dsDNA cartoon and ssDNA path (yellow spheres) from the Y DNA–FANCI maps, as well as their models on FANCD2, positioned by superimposing solenoids 3 and 4 of the two paralogs. The electrostatic potential was calculated with Adaptive Poisson-Boltzmann Solver (APBS) (*25*) and illustrated (–8 to +8 kT) with PyMOL (*26*).

References and Notes

1. G. L. Moldovan, A. D. D'Andrea, *Annu. Rev. Genet.* **43**, 223 (2009).
2. W. Wang, *Nat. Rev. Genet.* **8**, 735 (2007).
3. Y. Kee, A. D. D'Andrea, *Genes Dev.* **24**, 1680 (2010).
4. M. Räschle *et al.*, *Cell* **134**, 969 (2008).
5. P. Knipscheer *et al.*, *Science* **326**, 1698 (2009); 10.1126/science.1182372.
6. X. Shen *et al.*, *Mol. Cell* **35**, 716 (2009).
7. M. Ben-Yehoyada *et al.*, *Mol. Cell* **35**, 704 (2009).

8. C. Timmers *et al.*, *Mol. Cell* **7**, 241 (2001).
9. A. Smogorzewska *et al.*, *Cell* **129**, 289 (2007).
10. A. E. Sims *et al.*, *Nat. Struct. Mol. Biol.* **14**, 564 (2007).
11. J. C. Dorsman *et al.*, *Cell. Oncol.* **29**, 211 (2007).
12. M. Ishiai *et al.*, *Nat. Struct. Mol. Biol.* **15**, 1138 (2008).
13. A. R. Meetei *et al.*, *Nat. Genet.* **35**, 165 (2003).
14. I. Garcia-Higuera *et al.*, *Mol. Cell* **7**, 249 (2001).
15. A. Shimamura *et al.*, *Blood* **100**, 4649 (2002).
16. K. N. Yamamoto *et al.*, *Proc. Natl. Acad. Sci. U.S.A.* **108**, 6492 (2011).
17. A. Smogorzewska *et al.*, *Mol. Cell* **39**, 36 (2010).
18. W. H. Park *et al.*, *J. Biol. Chem.* **280**, 23593 (2005).
19. S. Longerich, J. San Filippo, D. Liu, P. Sung, *J. Biol. Chem.* **284**, 23182 (2009).
20. F. Yuan, J. El Hokayem, W. Zhou, Y. Zhang, *J. Biol. Chem.* **284**, 24443 (2009).
21. Fanconi Anemia Mutation Database, www.rockefeller.edu/fanconi/
22. J. M. Winget, T. Mayor, *Mol. Cell* **38**, 627 (2010).
23. M. A. Cohn *et al.*, *Mol. Cell* **28**, 786 (2007).
24. Single-letter abbreviations for the amino acid residues are as follows: A, Ala; C, Cys; D, Asp; E, Glu; F, Phe; G, Gly; H, His; I, Ile; K, Lys; L, Leu; M, Met; N, Asn; P, Pro; Q, Gln; R, Arg; S, Ser; T, Thr; V, Val; W, Trp; and Y, Tyr.
25. N. A. Baker, D. Sept, S. Joseph, M. J. Holst, J. A. McCammon, *Proc. Natl. Acad. Sci. U.S.A.* **98**, 10037 (2001).
26. The PyMOL Molecular Graphics System, version 1.3, Schrödinger, LLC (2010); www.pymol.org.

Acknowledgments: We thank D. King for mass spectroscopy analysis and the staff of the Advanced Photon Source Northeast Collaborative Access Team and National Synchrotron Light Source X29 beamlines for help with data collection. This work was supported by the NIH and the Howard Hughes Medical Institute. Coordinates and structure factors have been deposited with the Protein Data Bank (accession codes 3S51 for FANCI, 3S4W for FANCI-FANCD2, and 3S4Z for Y DNA-FANCI).

Supporting Online Material

www.sciencemag.org/cgi/content/full/333/6040/312/DC1
Materials and Methods
Figs. S1 to S12
Tables S1 to S3
References

18 March 2011; accepted 31 May 2011
10.1126/science.1205805

REPORTS

Detection of Convective Downflows in a Sunspot Penumbra

G. B. Scharmer,[1]* V. M. J. Henriques,[1] D. Kiselman,[1] J. de la Cruz Rodríguez[2]

The fine structure and dynamics of sunspots and the strong outflow in their outer filamentary part—the penumbra—have puzzled astronomers for more than a century. Recent theoretical models and three-dimensional numerical simulations explain the penumbral filaments and their radiative energy output as the result of overturning convection. Here, we describe the detection of ubiquitous, relatively dark downward flows of up to 1 kilometer per second (km/s) in the interior penumbra, using imaging spectropolarimetric data from the Swedish 1-meter Solar Telescope. The dark downflows are omnipresent in the interior penumbra, distinguishing them from flows in arched flux tubes, and are associated with strong (3 to 3.5 km/s) radial outflows. They are thus part of a penumbral convective flow pattern, with the Evershed flow representing the horizontal component of that convection.

A sunspot consists of a central dark umbra with intermittent bright dots and a surrounding extended filamentary penumbra (Fig. 1). The penumbra shows a complex dynamic fine structure with azimuthally strongly variable radial (Evershed) outflows (*1*), magnetic field strength, and field inclination. When observed even at high spatial resolution, the penumbral flows appear to consist of primarily radial outflows, upflows in the inner penumbra, and outflows in the outer penumbra, consistent with a description in terms of flows in arched flux tubes (*2*). However, such tubes cannot carry the energy needed to supply radiative losses; only convective vertical flows can do that (*3*–*8*). Recent models (*4*, *5*) and simulations (*6*–*9*) explain the filamentary structure as the result of overturning convection, with the symmetry broken by the inclined magnetic field and the Evershed flow corresponding to the horizontal component of that convection (*10*). Filament dynamics in sunspots observed well away from the solar disk center give some support to the convection models (*11*–*14*), but direct evidence for convection—a system of both upflows and

[1]Institute for Solar Physics of the Royal Swedish Academy of Sciences, and Department of Astronomy at Stockholm University, AlbaNova University Center, SE-10691 Stockholm, Sweden. [2]Institute for Theoretical Astrophysics, University of Oslo, Post Office Box 1029 Blindern, 0315 Oslo, Norway.
*To whom correspondence should be addressed. E-mail: scharmer@astro.su.se

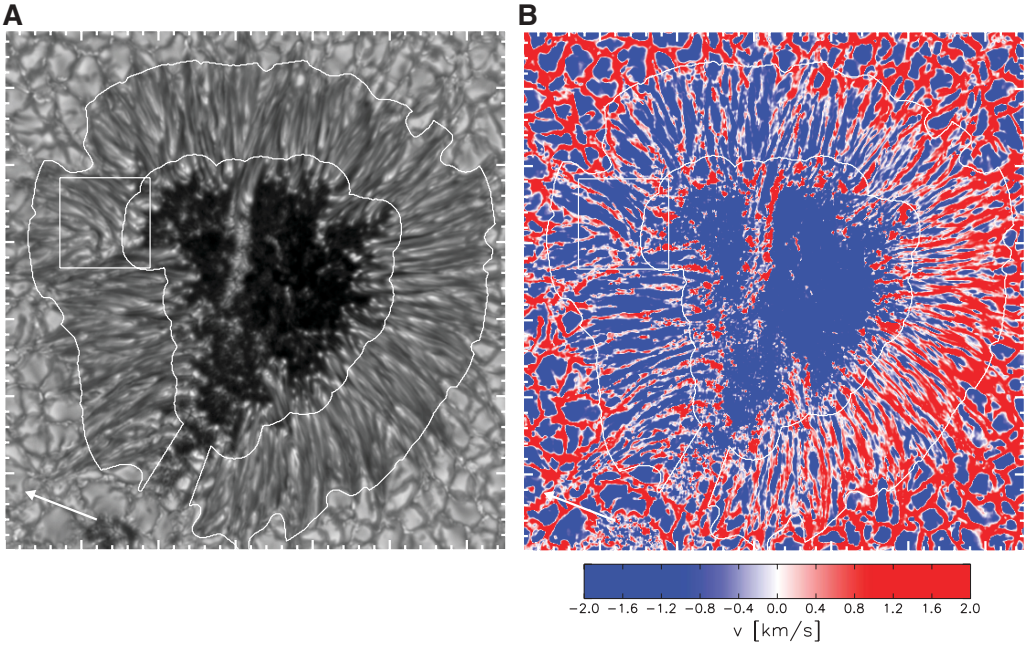

Fig. 1. Continuum image (**A**) and Doppler map (**B**) of the part of the field of view (FOV) containing the sunspot and its immediate surroundings, color-coded such that blue corresponds to motions toward and red away from the observer. The white contour outlines the region analyzed for convective flows; we refer to this as the "interior penumbra." The arrow points in the direction of the center of the solar disk (the direction to the observer). The overall blue color on the left and red on the right parts of the spot are mostly from strong horizontal (Evershed) flows. Superimposed on these flows are local upflows and downflows. A light bridge protrudes into the dark part of the sunspot from the upper part of the penumbra. Tick marks are in arc seconds; the FOV covers ~33 by 34 arc sec.

Structure of the FANCI-FANCD2 Complex: Insights into the Fanconi Anemia DNA Repair Pathway

Woo Joo, Guozhou Xu, Nicole S. Persky, Agata Smogorzewska, Derek G. Rudge, Olga Buzovetsky, Stephen J. Elledge and Nikola P. Pavletich

Science **333** (6040), 312-316.
DOI: 10.1126/science.1205805